An Improved Deep Learning Scheme for Solving 2D and 3D Inverse Scattering Problems

Yulong Zhou, *Student Member, IEEE*, Yu Zhong, Zhun Wei, Tiantian Yin and Xudong Chen, *Fellow, IEEE*

***Abstract*—Reconstructing the exact electromagnetic property of unknown targets from the measured scattered field is challenging due to the intrinsic nonlinearity and ill-posedness. In this paper, a new scheme, named the modified contrast scheme (MCS), is proposed to tackle nonlinear inverse scattering problems (ISPs). A local-wave amplifier coefficient is used to form the modified contrast, which is able to alleviate the global nonlinearity in original ISPs without decreasing the accuracy of the problem formulation. Moreover, the modified contrast is more suitable to be the input of the deep learning scheme, due to the unity bound of the modified contrast. Numerical results show that MCS with the modified contrast input performs well in both two-dimensional (2D) and three-dimensional (3D) testing examples in real time after offline training process, even in high relative permittivity cases. Compared with the dominant current scheme, a significant improvement is achieved in reconstructing high contrast scatterers.**

***Index Terms*—Inverse scattering problems, modified contrast scheme (MCS), deep learning, two-dimensional and three-dimensional**

I. Introduction

Inverse scattering problems (ISPs) aim to retrieve the nature of the unknown object in the domain of interest from the measured scattering data. The imaging technique based on ISPs plays an important role in various areas, such as non-destructive examination, remote sensing and biomedical imaging [1]–[6]. Due to the intrinsic nonlinearity and ill-posedness of ISPs, the accurate result is hard to be reconstructed from noise-contaminated measured data [7].

Inverse scattering algorithms can be divided into two categories. The first one is non-iterative algorithms with regularization method [8]–[12], which are able to obtain a good reconstruction result after making some reasonable approximation. The drawback of these non-iterative methods is that they are applicable only to weak scatterers. The second one is iterative algorithms with regularization method [13]–[22]. By minimizing the misfit between the calculated and measured data in the cost function, better reconstruction results can be obtained iteratively. Moreover, the efficiency of inversion procedure can be increased by using multi-resolution method [23]. However, these algorithms usually take a large amount of time in reconstruction procedure.

In recent years, learning by examples (LBE) techniques have been utilized to solve the ISP. The supervised descent method is trained in iterative least-square fashion from the training set [24]. Along with the progress in the deep learning algorithm, it exhibits extraordinary performance in various areas, which attracts many researchers' interest (see [25] and the reference therein). The convolution neural network (CNN) can be utilized to learn different kinds of relationships between the input and the output, like induced current [26] and contrast [27]–[29]. CNN could also be used to assist the iterative optimization method, which produces satisfactory results of two-dimensional (2D) high permittivity objects [30], [31]. Moreover, CNN can be extended to solve three-dimensional (3D) ISPs, where the input is the estimated contrast obtained through Born approximation [32].

Inspired by [18], a new scheme, named the modified contrast scheme (MCS), is proposed to reconstruct both 2D and 3D target objects with high contrast. Here, by high contrast, we mean that the contrast of scatterer reaches a level so that state-of-the-art pixel-based inversion algorithms have great difficulties to successfully obtain the reconstruction. The computational complexity of MCS is at the same level as the dominant current scheme (DCS) proposed in [28]. The numerical and experimental results show that the proposed MCS with the modified contrast input presents a good performance in reconstructing both 2D and 3D targets with high contrast. The main contributions of this paper are listed as follows. Firstly, the proposed scheme performs well when it reconstructs the scatterer with high contrast without adding extra computation cost. Compared with DCS, the proposed MCS with the modified contrast input presents a better generalization ability and is able to reconstruct scatterers with higher contrast. Secondly, the ambiguous part of the induced current (APIC) itself becomes an unknown in MCS, which could remedy the error existing in the dominant part of the induced current (DPIC), and also reduce the computational cost in the APIC generation. Thirdly, after introducing the local-wave amplifier coefficient, the modified contrast is more suitable to be an input of the deep learning scheme due to its unity bound, even when the relative permittivity of scatterer becomes large. Finally, we have provided 3D inversion data using deep learning, which is rare in the literature. Since most real-world ISPs are 3D ones, our presented 3D real-time inversion results can be chosen as a benchmark for researchers in ISP community to compare with.

The structure of this paper is listed as follows. Section II presents the formulation of the forward problem and the inverse problem, the implementation of the MCS, the

Manuscript received XXX. (Corresponding author: Xudong Chen.).

Y. Zhou, T. Yin, X. Chen are with the Department of Electrical and Computer Engineering, National University of Singapore, 117583 Singapore (e-mail: e0338289@u.nus.edu; e0021489@u.nus.edu; elechenx@nus.edu.sg).

Y. Zhong is with the Institute of High Performance Computing, A*STAR, 138632 Singapore (e-mail: zhongyu@ihpc.a-star.edu.sg).

Z. Wei is with the Key Laboratory of Micro-Nano Electronics and Smart System of Zhejiang Province, College of Information Science and Electronic Engineering, Zhejiang University, Hangzhou, China. (e-mail: weizhun1010@gmail.com).

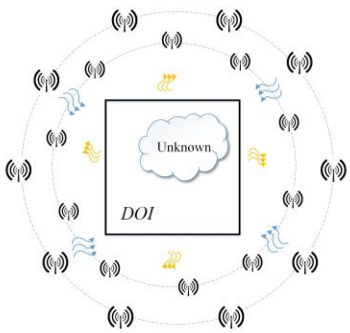

Fig. 1. Typical simulation setup of 2D inverse scattering problems.

architecture of the deep learning algorithm and the computation complexity of the proposed method. Section III shows the numerical comparison results between the MCS and DCS. MCS with different inputs are also investigated in this section. Then the extension of MCS to 3D reconstruction is given in Section IV. Section V shows the inversion results of experiment data by MCS. The conclusion is made in section VI.

II. Modified Contrast Scheme for 2D ISPs

For the convenience of understanding and description, a 2D transverse magnetic (TM) case is given, where the invariant longitude is along the z-direction. As demonstrated in Fig. 1, nonmagnetic scatterers are placed in the rectangular domain of interest (DOI) D, where the background is free space. Time-harmonic dependence as exp($-i\omega t$) is implied. Scatterers are illuminated by a number of N_i plane waves with electric fields E_p^i, p = 1, 2, …, N_i, from different incident angles. The scattered fields for each incidence are measured by N_r receivers located at $\mathbf{r}_q$, q = 1, 2, …, N_r, along a full circular line outside D, referred to as the measurement surface S.

The proposed MCS adopts the U-Net architecture that will be presented in Section II C. Since both training and testing stages require to generate fast the input of neural network, we only run a few iterations when minimizing the objective function, which will be detailed in Section II B. Here, we denote one-dimensional vector as $\bar{a}$, and 2D tensor as $\bar{\bar{a}}$.

A. *Forward Problem*

The forward problem can be written into two formulas:

$$E^t(\mathbf{r}) = E^i(\mathbf{r}) + \int_D G^{2D}(\mathbf{r},\mathbf{r}')I(\mathbf{r}')d\mathbf{r}', \text{ for } \mathbf{r}\in D \tag{1}$$

$$E^s(\mathbf{r}) = \int_D G^{2D}(\mathbf{r},\mathbf{r}')I(\mathbf{r}')d\mathbf{r}', \quad \text{for } \mathbf{r}\in S \tag{2}$$

Equation (1) is the field equation. E^t denotes the total electric field. G^{2D} is the Green's function for 2D TM case. The induced contrast current (ICC) $I(\boldsymbol{r})$ in D is defined as $I(\boldsymbol{r}) = \chi(\boldsymbol{r})E^t(\boldsymbol{r})$ with the contrast $\chi(\boldsymbol{r}) = \varepsilon_r(\boldsymbol{r}) - 1$. Equation (2) is the data equation. E^s denotes the scattering electric field on the measurement surface S. As in [18], a modified contrast $R(\boldsymbol{r}) = \beta(\boldsymbol{r})\chi(\boldsymbol{r})[\beta(\boldsymbol{r})\chi(\boldsymbol{r}) + 1]^{-1}$ is proposed to multiply both sides of (1), then the contraction integral equation for inversion (CIE-I) can be obtained:

$$\begin{aligned}\beta(\mathbf{r})I(\mathbf{r}) &= R(\mathbf{r})\beta(\mathbf{r})I(\mathbf{r})\\ &+R(\mathbf{r})\left[E^i(\mathbf{r}) + \int_D G^{2D}(\mathbf{r},\mathbf{r}')I(\mathbf{r}')d\mathbf{r}'\right], \quad \text{for } \mathbf{r}\in D\end{aligned} \tag{3}$$

where β is a local-wave amplifier coefficient that amplifies the introduced term $R(\boldsymbol{r})\beta(\boldsymbol{r})I(\boldsymbol{r})$. To differentiate this term from the global term $R(\boldsymbol{r})\int_D G^{2D}(\boldsymbol{r},\boldsymbol{r}')I(\boldsymbol{r}')d\boldsymbol{r}'$, which means multiple scattering via the Green's function $G^{2D}(\boldsymbol{r},\boldsymbol{r}')$, this newly introduced term is called the local term, since the induced current at a position does not depend on another position in this term. Compared with (1), where the local term is $E^i(\boldsymbol{r})$ and the global term is $\int_D G^{2D}(\boldsymbol{r},\boldsymbol{r}')I(\boldsymbol{r}')d\boldsymbol{r}'$, (3) contains more portion of local term controlled by the value of β. The larger the value of β, the stronger the local effect.

The goal of ISPs is to identify the unknown permittivity of scatterers by minimizing the misfit between the measured scattering electric field and the calculated one. Since the objective function is nonlinear, the minimization problem is usually solved by iterative algorithms. Due to the intrinsic instability and nonlinearity in ISPs, regularization method is used to balance between accuracy and stability of the solution. Such an optimization procedure can be formulated as follows:

$$Min: f(\varepsilon_r) = \sum_{p=1}^{N_i}\left\|L\left(E_p^i,\varepsilon_r\right) - E_p^s\right\|^2 + \alpha T(\varepsilon_r) \tag{4}$$

where L is denoted as the forward problem solver, T is denoted as the regularization function, and α is the constant regularization coefficient.

B. *Iteration Procedure in MCS*

Here, the DOI is discretized into $M \times M$ subunits to apply the method of moment (MOM) with the pulse basis function and the delta test function, and the center of each subunit is located at $\mathbf{r}_n$, n = 1, 2, …, M^2. After discretization, the discretized form of (2) and (3) is obtained [18]:

$$\bar{E}^s = \bar{\bar{G}}_S^{2D}\cdot\bar{I} \tag{5}$$

$$\text{diag}(\bar{\beta})\cdot\bar{I} = \text{diag}(\bar{R})\cdot\left[\text{diag}(\bar{\beta})\cdot\bar{I} + \bar{E}^i + \bar{\bar{G}}_D^{2D}\bar{I}\right] \tag{6}$$

where $\bar{\beta}$, $\bar{R}$, $\bar{I}$ and $\bar{E}^i$ are $M^2 \times 1$ vectors, and diag(•) is the operator that returns a square diagonal matrix with the elements of the vector on the main diagonal. $\bar{\bar{G}}_D^{2D}$ is an $M^2 \times M^2$ matrix that maps the ICC to the scattered field in D, and $\bar{\bar{G}}_S^{2D}$ is an $N_r \times M^2$ matrix that maps the ICC to the scattering field on S.

Following the convention in [17], the ICC $\bar{I}$ in (5) and (6) could be divided into two parts, which are located in two orthogonal and complementary subspaces spanned by the singular vectors of $\bar{\bar{G}}_S^{2D}$. One is DPIC $\bar{I}^d$ within large singular value subspace, and the other is APIC $\bar{I}^a$ within small and null singular value subspace. The result of a singular value decomposition on $\bar{\bar{G}}_S^{2D}$ is that $\bar{\bar{G}}_S^{2D} = \sum_n \bar{u}_n\sigma_n\bar{v}_n^H$, where $\bar{u}_n$ denotes the nth left singular vector, σ_n denotes the nth singular value, $\bar{v}_n$ denotes the nth right singular vector and the superscript H denotes the Hermitian operator, i.e., complex conjugate transpose. Given the orthogonality of the singular vectors, the DPIC $\bar{I}^d$ can be calculated from first L large singular values and is given as

$$\bar{I}^{\mathrm{d}} = \sum_{n=1}^{L}\frac{\left(\bar{u}_n^H\cdot\bar{E}^s\right)}{\sigma_n}\bar{v}_n, \tag{7}$$

Different from utilizing FFT-TSOM to generate the APIC $\bar{I}^a$ mentioned in [18], we choose the APIC $\bar{I}^a$ itself as the unknown. The advantages of such a modification are listed as follows. The first one has to do with the appropriate input generation for the neural network. For this purpose, we implement only two iterations to minimize the objective function. In this situation, we prefer using APIC itself instead of only low-frequency Fourier bases as adopted in FFT-TSOM. Another advantage is that it will cost less time in the iteration procedure of MCS, due to the omission of the APIC generation procedure in FFT-TSOM. After replacing $\bar{I}$ in (5) and (6) by $\bar{I}^d$ and $\bar{I}^a$, a cost function for $\bar{I}_p^a$ for pth incidence and $\bar{R}$ can be obtained:

$$f\left(\bar{I}_1^a, \bar{I}_2^a, \ldots, \bar{I}_{N_i}^a, \bar{R}\right) = \sum_{p=1}^{N_i}\left(\frac{\left\|\bar{\bar{A}}\cdot\bar{I}_p^a + \bar{B}_p\right\|^2}{\left\|\bar{E}_p^i\right\|^2} + \frac{\left\|\bar{\bar{G}}_s^{2D}\cdot\bar{I}_p^a + \bar{\bar{G}}_s^{2D}\cdot\bar{I}_p^d - \bar{E}_p^s\right\|^2}{\left\|\bar{E}_p^s\right\|^2}\right) \quad (8)$$

where

$$\begin{aligned}\bar{\bar{A}} &= \operatorname{diag}\left(\bar{\beta}\right) - \operatorname{diag}\left(\bar{R}\right)\cdot\left[\operatorname{diag}\left(\bar{\beta}\right) + \bar{\bar{G}}_D^{2D}\right]\\ \bar{B}_p &= \operatorname{diag}\left(\bar{\beta}\right)\cdot\bar{I}_p^d - \operatorname{diag}\left(\bar{R}\right)\cdot\left[\operatorname{diag}\left(\bar{\beta}\right)\cdot\bar{I}_p^d + \bar{\bar{G}}_D^{2D}\cdot\bar{I}_p^d + \bar{E}_p^i\right]\end{aligned} \quad (9)$$

As mentioned in [18], the reconstructed contrast by the noniterative back-propagation (BP) method is reliable when scatterers in D are weak. However, when scatterers become stronger, the BP result is far from the true contrast, even misleading. To avoid such an influence, the homogeneous background medium is set to be the initial guess of the scatterer profile. The Polak-Ribière conjugate gradient method [16] is used to update the APIC $\bar{I}^a$ and the modified contrast $\bar{R}$ alternatively.

Since the purpose of minimizing the objective function (8) is to generate the input of the neural network, we need to only run a few iterations so that it is time-saving in both training and testing stages. The implementation is listed as follows:

Step 1: $n = 0$: Choose the background medium as the initial guess of $\bar{R}_0$; $\bar{I}_{p,0}^a = 0$; the search direction $\bar{\rho}_{p,0} = 0$.

Step 2: $n = 1$.

Step 2.1: Update $\bar{I}_{p,n}^a$: Calculate gradient $\bar{g}_{p,n} = \nabla_{\bar{I}_p^a} f$ evaluated at $\bar{I}_{p,n-1}^a$ and $\bar{R}_{n-1}$ and written as

$$\bar{g}_{p,n} = \frac{\left(\bar{\bar{G}}_s^{2D}\right)^H\cdot\left[\bar{\bar{G}}_s^{2D}\cdot\bar{I}_p^a + \bar{\bar{G}}_s^{2D}\cdot\bar{I}_p^d - \bar{E}_p^s\right]}{\left\|\bar{E}_p^s\right\|^2} + \frac{\bar{\bar{A}}^H\cdot\left[\bar{\bar{A}}\cdot\bar{I}_p^a + \bar{B}_p\right]}{\left\|\bar{E}_p^i\right\|^2}; \quad (10)$$

Calculate the search direction $\bar{\rho}_{p,n} = \bar{g}_{p,n} + \frac{\operatorname{Re}\left[\left(\bar{g}_{p,n} - \bar{g}_{p,n-1}\right)^H\cdot\bar{g}_{p,n}\right]}{\left\|\bar{g}_{p,n-1}\right\|^2}\bar{\rho}_{p,n-1}$. The scalar $d_{p,n}$ is defined by $\bar{I}_{p,n}^a = \bar{I}_{p,n-1}^a + d_{p,n}\bar{\rho}_{p,n}$ and the minimizer is $d_{p,n} = Num/Den$, where the numerator and denominator are

$$\begin{aligned}Num &= -\left(\bar{\rho}_{p,n}\right)^H\cdot\bar{g}_{p,n},\\ Den &= \frac{\left\|\bar{\bar{G}}_s^{2D}\cdot\bar{\rho}_{p,n}\right\|^2}{\left\|\bar{E}_p^s\right\|^2} + \frac{\left\|\bar{\bar{A}}\cdot\bar{\rho}_{p,n}\right\|^2}{\left\|\bar{E}_p^i\right\|^2},\end{aligned} \quad (11)$$

respectively.

Step 2.2: Update $\bar{R}_n$: Update (8) with the updated APIC $\bar{I}_p^a$. Then the function becomes quadratic in terms of $\bar{R}_n$ for the mth cell and the solution is

$$\bar{R}_n(m) = \left[\sum_{p=1}^{N_i}\left(\bar{\psi}_{p,n}(m)\right)^*\cdot\left[\bar{\beta}(m)\cdot\bar{I}_{p,n}(m)\right]\right] / \left[\sum_{p=1}^{N_i}\left|\bar{\psi}_{p,n}(m)\right|^2\right] \quad (12)$$

in which $\bar{\psi}_{p,n} = diag(\bar{\beta})\cdot\bar{I}_{p,n} + \bar{\bar{G}}_D^{2D}\cdot\bar{I}_{p,n} + \bar{E}_p^i$, and * denotes the conjugate operation.

Step 3: $n = 2$.

Step 3.1: Update $\bar{I}_{p,n}^a$: Re-execute Step 2.1 with the updated $\bar{R}_n$.

Step 3.2: Update $\bar{R}_n$: Update (8) with the updated APIC $\bar{I}_p^a$. We then calculate the $\bar{R}_{p,n}$ for mth cell of pth incidence as the minimizer of (8) and the solution is

$$\bar{R}_{p,n}(m) = \left[\left(\bar{\psi}_{p,n}(m)\right)^*\cdot\left[\bar{\beta}(m)\cdot\bar{I}_{p,n}(m)\right]\right] / \left|\bar{\psi}_{p,n}(m)\right|^2. \quad (13)$$

For the convenience of implementation, the value of $\bar{\beta}(m)$ is chosen to be a constant β_0 for all subunits. The influence of the global nonlinearity $\bar{\bar{G}}_D^{2D}\cdot\bar{I}^a$ can be suppressed by choosing a large value β_0.

It is important to discuss the motivation of using modified contrast scheme. Firstly, compared with the DCS model mentioned in [28], the nonlinearity of the problem caused by multiple scattering can be alleviated without sacrificing the accuracy of the physical model. A large value of β gives more weight to local terms, i.e., the multiple scattering term is depressed, and consequently, the inversion for a large value β is close in spirit to Born approximation that is a well-known linear inversion model. For more details, please refer to [18]. Secondly, the value range of the modified contrast function R is between 0 and 1 if β_0 has a positive real part and a nonpositive imaginary part, and such a unity bound would facilitate the learning process of the neural network, which makes it more suitable to be the input of the neural network.

C. *U-Net Deep Learning Architecture in MCS*

Here, the U-Net deep learning architecture adopted in [33] is selected as the backbone of the learning scheme in MCS. As illustrated in Fig. 2, the U-Net architecture can be divided into two branches, the extracting branch and expanding branch. The extracting branch consists of the convolution block (*3×3* convolution kernels with *1×1* convolution stride, batch normalization and rectified linear unit) and the down-sampling model (*2×2* max-pooling unit). The expanding branch consists of the convolution block and the up-sampling model (*2×2*

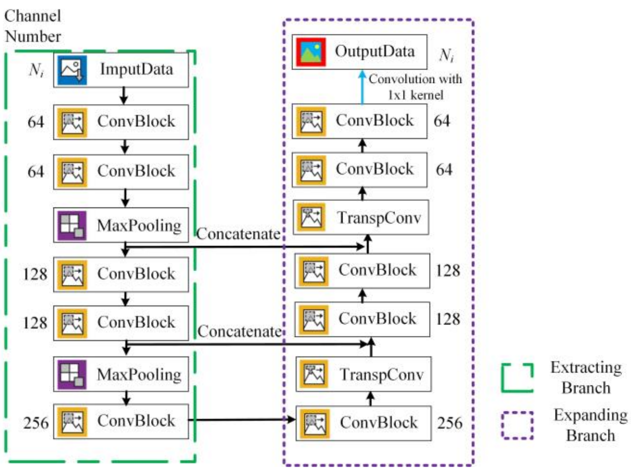

Fig. 2. U-Net architecture.

transposed convolution kernels with 2×2 convolution stride). Moreover, the result of the convolution model in the extracting branch is concatenated with the result of the up-sampling model in the expanding branch to improve the reconstruction speed in the expanding branch. The mean square error (MSE) [34] is selected as the cost function, and ADAM is chosen as the optimizer [35].

As for the deep learning process, there are two options for the input and the output of each channel of the U-Net deep learning architecture. One is the contrast $\bar{\bar{\chi}}_p = ten\{\bar{\chi}_p\}$ that is further derived from the modified contrast in (13), and the exact contrast is the label of the U-Net, where $ten\{\bullet\}$ denotes an operation that obtains an $M \times M$ matrix by reshaping an $M^2 \times 1$ vector. The other one is the new modified contrast $\bar{\bar{R}}_p = ten\{\bar{R}_p\}$ with a new constant value β_0, where $\bar{R}_p$ is obtained from the definition $\bar{R}_p(m) = \beta_0\bar{\chi}_p(m)[\beta_0\bar{\chi}_p(m)+1]^{-1}$, and the corresponding exact modified contrast is set as the label of the U-Net. The new constant value β_0 for the input generation provides us a freedom to control the performance of the U-Net. The MCS with the contrast input and output is referred to as MCSC, and the MCS with the new modified contrast input and output is referred to as MCSM. There are two main differences between the inputs of MCSC and MCSM. The first one is the physical meaning. The other one is the value range of the input. The differences are summarized in Table I. For comparison, the MCSC and MCSM inputs of the high contrast profile are shown in Fig. 3.

D. Computational Complexity

For the MCS, the computational complexity is $O(N_i M^2 \log M^2)$ when computing $\bar{\bar{G}}_D^{2D} \cdot \bar{I}$ in (10) via FFT algorithm. In order to get the DPIC $\bar{I}^d$ in (7), a thin SVD is implemented on $\bar{\bar{G}}_s^{2D}$ and the computational complexity is $O(N_r^2 M^2)$. Compared with DCS, the computational cost of the APIC $\bar{I}^a$ generation is avoided.

For the U-Net model, the major computational complexity is the convolution unit. For example, if the map size and convolution kernel size are $M_z \times M_z$ and $K_z \times K_z$ respectively, the number of input feature maps and output feature maps are P_i and P_o respectively, then the computational complexity of the convolution is $O(P_i P_o M_z^2 K_z^2)$. For the first convolution block of U-Net in this paper, the value of P_i is the number of incidences N_i, the map size M_z is the discretization value M and K_z is 3 for the 3×3 convolution kernel. Such a computation can be accelerated by using GPU.

TABLE I
DIFFERENCES BETWEEN THE INPUTS OF MCSC AND MCSM

	MCSC	MCSM
Input Type	Contrast $\bar{\bar{\chi}}$	Modified Contrast $\bar{\bar{R}}$
Value Range	Can be either more than one or less than one	Always less than one

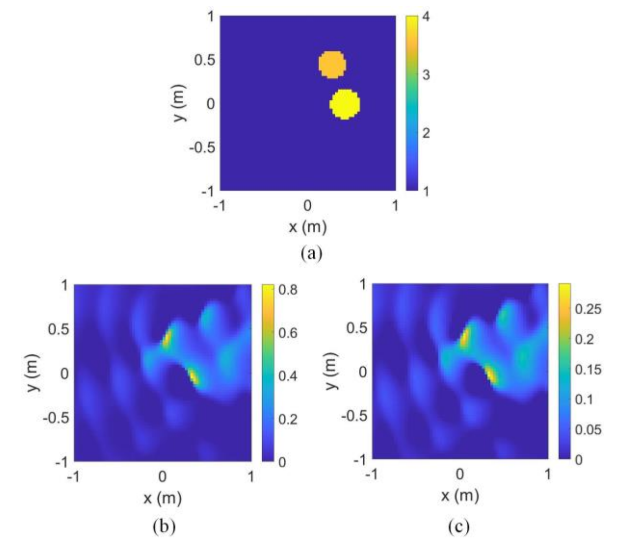

Fig. 3. The high contrast circular scatterer profile. (a) Ground truth. (b) MCSC input. (c) MCSM input.

III. 2D NUMERICAL RESULTS

In order to quantitatively evaluate the reconstruction performance of the proposed MCS in the inverse scattering problem, the difference between the target scatterer and the output of the U-Net is defined as the relative error (R_e), formulated as follows:

$$R_e = \sqrt{\frac{1}{M^2}\left[\sum_{r=1}^{M^2}\left|\frac{\bar{\varepsilon}(m)-\bar{\varepsilon}^{tr}(m)}{\bar{\varepsilon}(m)}\right|^2\right]} \tag{14}$$

where $\bar{\varepsilon}^{tr}$ is the true relative permittivity distribution of the scatterer, $\bar{\varepsilon}$ is the reconstructed result of the MCS, and M^2 is the total discretization number in DOI.

In the setup of the simulation, the size of DOI is 2×2 m^2. For the forward problem, the synthetic scattered fields are calculated by the MoM with $M = 100$. To avoid the inverse crime, a 64×64 discretization of D is implemented in the inverse problem. There are 16 incident plane waves and 32 line receivers evenly placed on the circle of radius 4λ centered at the coordinate origin, where λ is the wavelength in free space. The operating frequency is 400 MHz. Additive white Gaussian noise with a level of 5% has been added to the synthetic scattered electric field.

TABLE II
AVERAGE R_e OF DIFFERENT METHODS

	DCS	MCSM	MCSC
Example 1: Weak circular cylinder	3.59%	3.63%	3.80%
Example 2: Strong circular cylinder	23.92%	18.54%	21.9%
Example 3: MNIST	12.32%	11.91%	13.0%

For MCS, L is selected to be 15 following the standard mentioned in [28], and a large constant value $\beta_0 = 6$ is used in the MCS iteration procedure to obtain the modified contrast and consequently the contrast. The MCSC uses the so-obtained contrast as the input to predict the contrast as the output. In MCSM, U-Net chooses a new modified contrast as the input and output, where the new modified contrast is calculated from a small value of $\beta_0 = 0.5$, which is motivated by the gradually decreasing β adopted in [18]. To be specific, MCSM first runs two iterations that are presented in Section II.B with a large value of β_0 to generate the input of the U-Net, which contains low spatial-frequency component of the scatterer. Next, the U-Net aims to recover the high spatial-frequency component, and thus a small value of β_0 is needed in order to include the multiple scattering effect.

In the training process, Python 3.7 is used to implement the U-Net architecture. 500 epochs are executed on NVIDIA RTX 2060 GPU (6 GB), where each epoch costs approximately 15 seconds. In each epoch, 1900 training samples are used to train the U-Net, and 100 samples are used to validate the training performance. In the testing process, 20 new examples are selected to test the reconstruction ability of the U-Net, and each reconstruction result can be obtained within one second. For practical cases, the time cost for the training process can be further reduced by utilizing more powerful GPUs or parallel calculation. In Sections III A-B, neural networks deal with in-range cases, where test cases are within the range of training set. In Sections III C, the comparison between the MCSC and MCSM is discussed. To test the generalization ability, out-of-range cases are tested in Section III D.

A. Circular Cylinder Dataset

Here, circular cylinder samples randomly generated by MATLAB are used as the training profile. Due to the size limitation of DOI, the radius of random cylinders is between 0.15 and 0.4 m, and the number is between 1 and 3. The relative permittivity is also limited in a range to better compare the results in the same level of nonlinearity.

In Example 1, weak cylinders are chosen as the training samples and testing samples, the relative permittivity of which is between 1.5 and 2.0. As shown in Fig. 4, MCSM presents good reconstruction ability in weak scatterers as well as DCS, which are close to true profiles. The average R_e of 20 examples is listed in Table II. The value of average R_e demonstrates that the reconstruction performance of these two schemes is at the same level when being applied in weak scatterers.

In Example 2, stronger cylinders are used to train and test

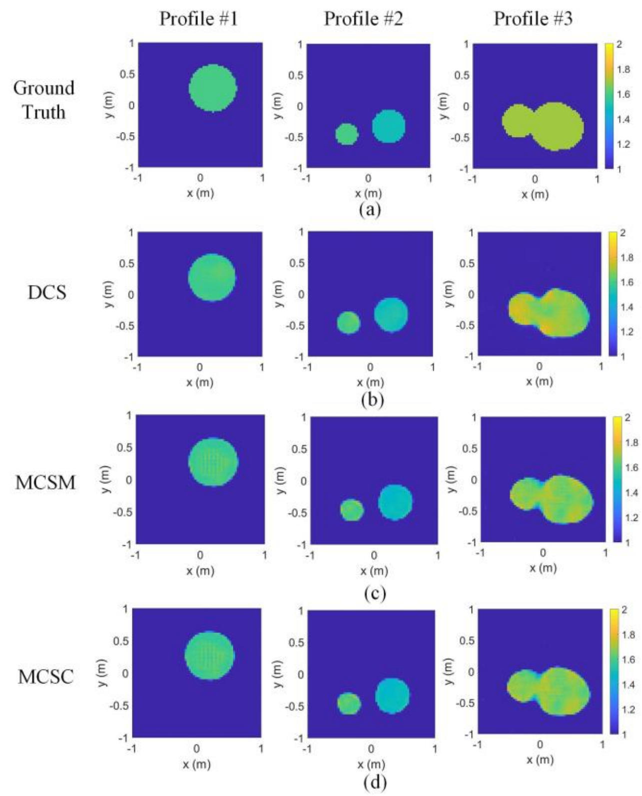

Fig. 4. Example 1: Reconstruction results of weak circular scatterer profiles. (a) Ground truth. (b) DCS results. (c) MCSM results. (d) MCSC results.

the U-Net, the relative permittivity of which is in the range from 3.5 to 4.0. According to Fig. 5(b), a large distortion exists in reconstruction results of DCS. The boundary of two scatterers is not reconstructed well in Test Profile#2 of DCS, and a large discrepancy appears in the reconstructed Test Profile#3 of DCS, which indicates the limitation of the DCS. It can be observed from Fig. 5(c), MCSM could still reconstruct the scatterer with satisfactory results. The relative error R_e of Example 2 is given in Table II. MCSM exhibits better performance than DCS when the relative permittivity of scatterers increases. There are two reasons for the better performance of MCSM for high contrast scatterers. The first is that MCSM utilizes APIC to a greater extent in the process of generating the input of neural network. Different from DCS, where APIC is approximated by low-frequency components, MCSM considers all frequency components. Moreover, a large value of β_0 used in generating the input of U-Net could suppress the global-wave behaviors and consequently reduce the nonlinearity caused by the stronger scatterers. Therefore, a good estimation of the contrast distribution can be obtained in limited iterative steps. The second reason is that the U-Net deals with a less nonlinear relationship between the input and output of MCSM than the counterpart of DCS, which in fact can be mathematically traced back to [18].

B. MNIST Dataset

The widely used dataset MNIST are also used as training and testing samples, denoted as Example 3 [36]. The digit is selected to represent scatterers with random relative

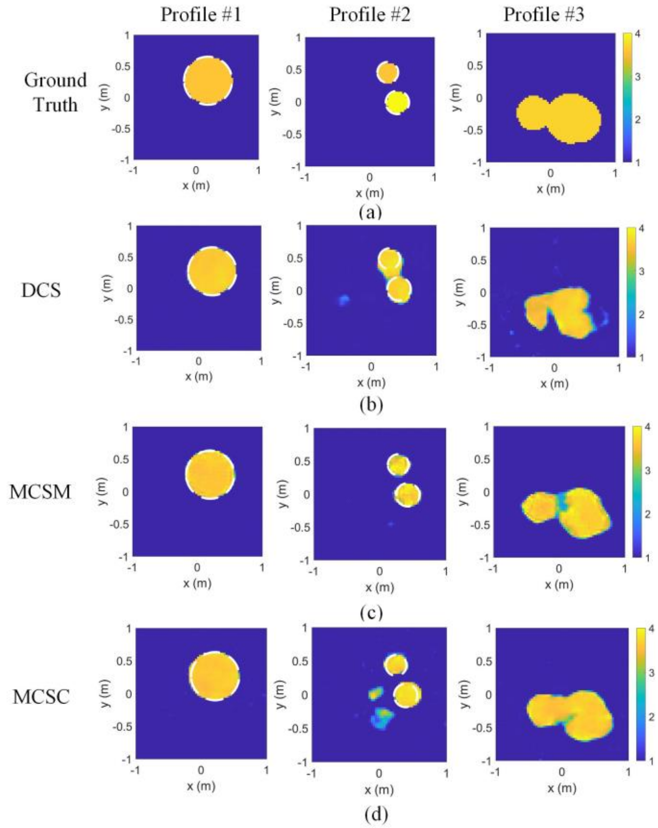

Fig. 5. Example 2: Reconstruction results of strong circular scatterer profiles. (a) Ground truth. (b) DCS results. (c) MCSM results. (d) MCSC results.

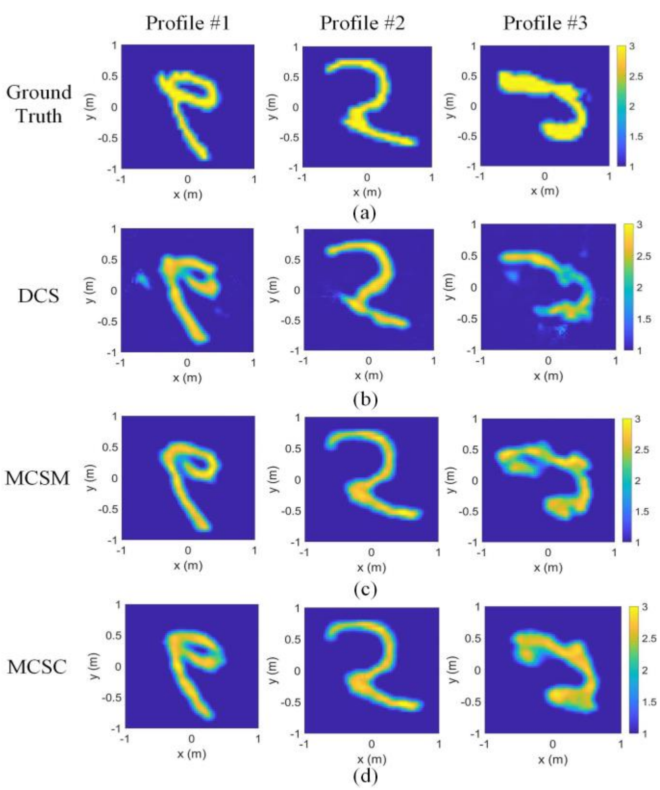

Fig. 6. Example 3: Reconstruction results of MNIST profiles. (a) Ground truth. (b) DCS results. (c) MCSM. (d) MCSC.

permittivity ranging from 2.5 to 3.0. Reconstructed digit profiles are illustrated in Fig. 6. Fig. 6 shows that both DCS and MCSM could generate satisfactory results, but some distortion appears in DCS results. The relative error R_e of Example 3 is given in Table II.

C. MCS performance with different inputs

To investigate the influence of the input on the U-Net architecture performance, reconstruction results by MCSC are also given in Examples 1-3. From the comparison between Fig. 4(c) and 4(d), the influence of the input is weak when scatterers in *D* is weak. With the relative permittivity of scatterers in *D* increasing, the input influence becomes more significant. As demonstrated in Fig. 5(c) and 5(d), some artifacts appear in the reconstruction Profile#2 via MCSC, while MCSM still offers a satisfactory reconstruction result. The average R_e of 20 examples is listed in Table II. Compared with MCSC, the modified contrast is more suitable to be the input of the U-Net architecture. The reason is that the value of the modified contrast is still less than one even when the relative permittivity of scatterers becomes stronger.

D. Generalization Ability

To further test the generalization ability of the MCSM, several profiles are used to test the network performance trained by Example 1. Such testing profiles are very different from training samples, which never appears in the training dataset. In Fig. 7(a), an Austria profile with ε_r=1.5 is used. The discrepancy between the reconstructed Austria via MCSM and true Austria profile is small. Although the gap between the ring and cylinders is unclear in the MCSM result, the relative error R_e is just 7.02%. For Fig. 7(b), circular cylinders within the range from 2.0 to 2.5 are utilized, which are higher than the range of training samples. MCSM could provide a satisfactory result while DCS presents a distorted one. To further verify the generalization ability of MCSM, MNIST within the range from 2.0 to 2.5 are selected, the shape and relative permittivity of which are both new to the trained network. As shown in Fig. 7(c), the shape and position of MNIST profile can still be reconstructed well by MCSM, even though the nonlinearity of the scatterer increases. To quantify discrepancy in reconstructed profiles, all R_e of MCSM results are calculated and given in Table III. It can be observed that MCSM outperforms DCS in terms of generalization ability.

IV. 3D Numerical Results

In 3D setup, the size of DOI is $1 \times 1 \times 1$ m^3. For the forward problem, the synthetic scattered fields are calculated by the MoM using a $32 \times 32 \times 32$ discretization. To avoid the inverse crime, a $16 \times 16 \times 16$ mesh of DOI is used in the inverse problem. There are 60 linearly-polarized transmitters and receivers evenly placed on three circles of radius 3 m centered at the coordinate origin, which are in x-y, y-z and x-z planes. In each circle, there are 20 linearly-polarized transmitters and receivers that are uniformly distributed on the circle. The

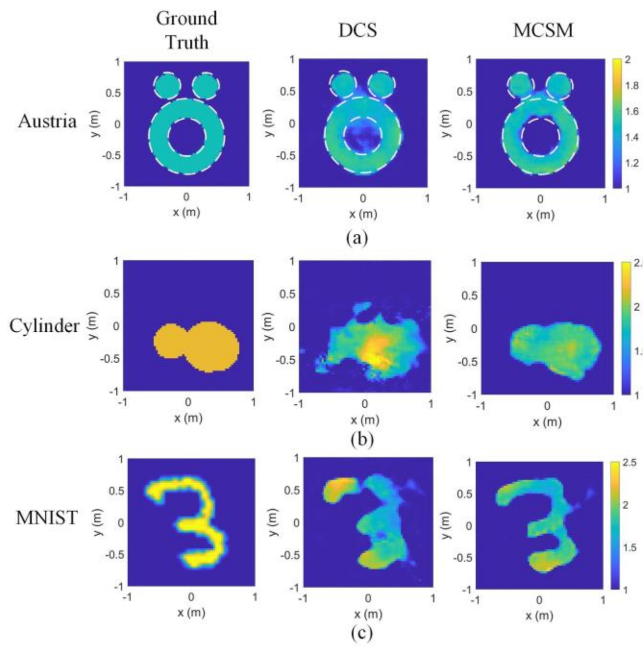

Fig. 7. Generalization ability. (a) Austria. (b) Cylinder. (c) MNIST.

TABLE III
R_e OF RECONSTRUCTED PROFILES SHOWN IN FIG. 7

	DCS	MCSM
Austria	8.13%	7.02%
Cylinder	19.82%	13.64%
MNIST	17.71%	9.14%

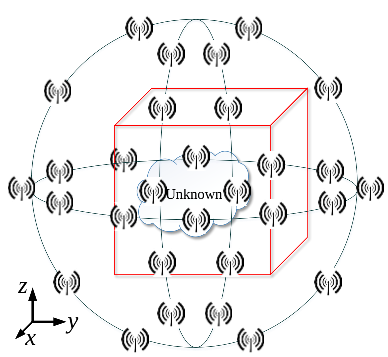

Fig. 8. Simulation setup for 3D ISPs, where the red cube is the DOI.

polarization of transmitters in the y-z plane is x-polarized, and those in the x-z and x-y planes are in the y- and z- polarized, respectively. The operating frequency is 300MHz. White Gaussian noise with a level of 5% is added to the synthetic scattered electric field. Here, L is selected to be 40. The setup for the numerical test is demonstrated in Fig. 8.

Here, 3D U-Net is used as the backbone of the deep learning algorithm for 3D ISPs [37]. The basic structure of 3D U-Net is similar to the 2D U-Net mentioned in Section II, like the layer number and the kernel number in each layer. In 3D U-Net, 3D convolution kernel (3×3×3), 3D max-pooling unit (2×2×2) and 3D transposed convolution kernel (2×2×2) are used. The sample number in 3D U-Net is the same as that stated in the 2D U-Net training process. The MSE is still selected as the cost function for training, and ADAM is chosen as the optimizer.

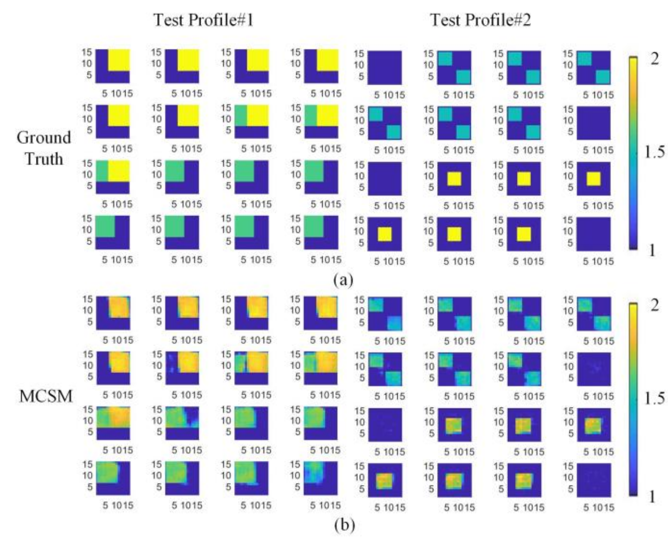

Fig. 9. Sectional view of 3D test cubic profiles. (a) Exact permittivity distribution. (b) Reconstructed permittivity distribution in the DOI. First row, from left to right, shows cross sections of the scatterer with section index p = 1 to 4; second row from left to right, shows cross sections of the scatterer with p = 5 to 8; and so forth. The x-axis and y-axis refer to the indexes of m and n, respectively.

A. *3D Inhomogeneous Cubic Scatterers*

To examine MCSM's ability to reconstruct 3D inhomogeneous objects, random 3D cubic scatterers with the relative permittivity range between 1.5 and 2.0 are firstly selected as the training sample. The edge length of random cubes is between 0.2 and 0.3 m, and the number is between 1 and 3. Only the sectional view of the reconstructed target by MCSM is presented in Fig. 9, due to the lack of DCS information in 3D sample reconstruction. It can be seen from Fig. 9(b) that cubic scatterers with different relative permittivity can be reconstructed by the proposed MCSM. Although the scatterer number increases in test profile #2, the boundary of each cubic scatterer is still reconstructed well, which indicates that the MCSM is able to reconstruct 3D inhomogeneous targets. The average R_e of 20 testing examples is only 9.86%.

B. *3D Homogeneous MNIST Scatterers*

To test MCSM's ability to reconstruct 3D object with high relative permittivity, random 3D MNIST is selected as the training sample. 3D MNIST is obtained by stretching the 2D MNIST sketch along z-axis. Then the obtained 3D MNIST is rotated by random degrees around an axis passing through the origin of coordinate. For better understanding, the generation procedure is illustrated in Fig. 10. The relative permittivity range of 3D MNIST model is set between 3.5 and 4.0. According to Fig. 11(b), although there is a discrepancy existing in the relative permittivity value of the MCSM reconstruction results, the shape and position of the target are reconstructed well, which indicates MCSM is still able to

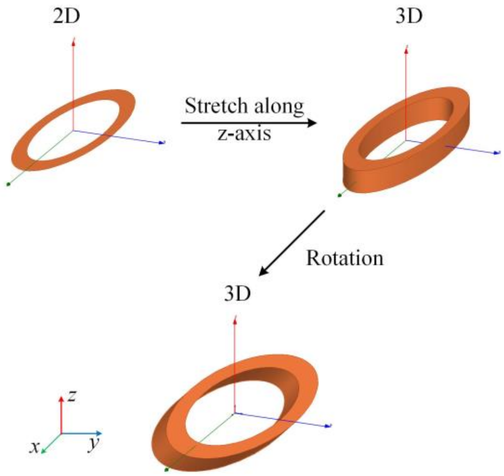

Fig. 10. The 3D MNIST generation procedure.

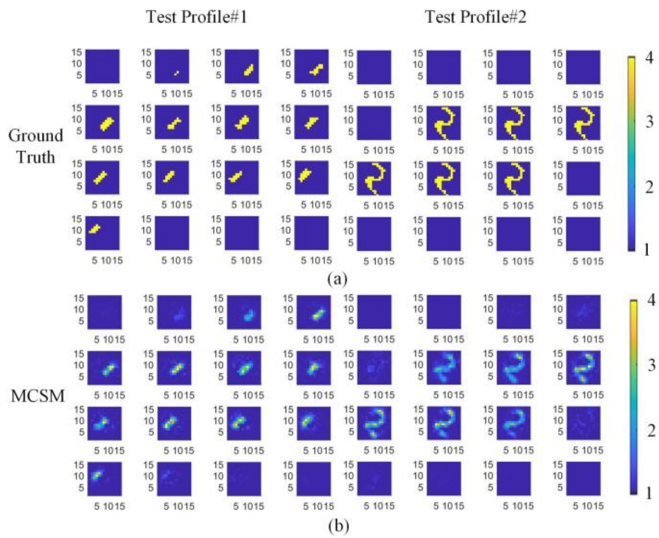

Fig. 11. Sectional view of 3D test MNIST profiles. (a) Exact permittivity distribution. (b) Reconstructed permittivity distribution in the DOI. The index of sections can be found in the caption of Fig. 9.

reconstruct 3D target with high contrast. The average R_e of 20 testing examples is 20.84%.

C. 3D Generalization Ability

In order to investigate the 3D generalization ability of the proposed MCSM, 3D MNIST objects that have different relative-permittivity ranges from the training range are utilized for testing. The selected relative-permittivity ranges of testing samples are from 3.0 to 3.5 and from 4.1 to 4.5, respectively. The former testing range is lower than the training range (from 3.5 to 4.0), whereas the latter is higher. The amount of testing samples for each relative-permittivity range is 20. The sectional view of reconstructed 3D MNIST profiles are presented in Fig. 12 and Fig. 13, respectively. The output of MCSM still performs well when tested by out-of-range 3D samples, indicating that the proposed MCSM could be a good candidate for fast 3D reconstruction. The respective average R_e are 20.45% for profiles within the range between 3.0 to 3.5 and 23.78% for profiles within the range between 4.1 to 4.5.

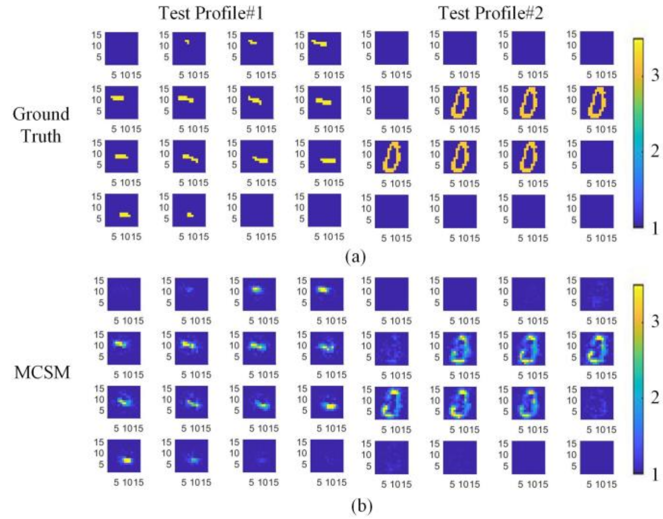

Fig. 12. Sectional view of reconstructed 3D MINIST with the relative permittivity range between 3.0 and 3.5. (a) Exact permittivity distribution. (b) Reconstructed permittivity distribution in the DOI. The index of sections can be found in the caption of Fig. 9.

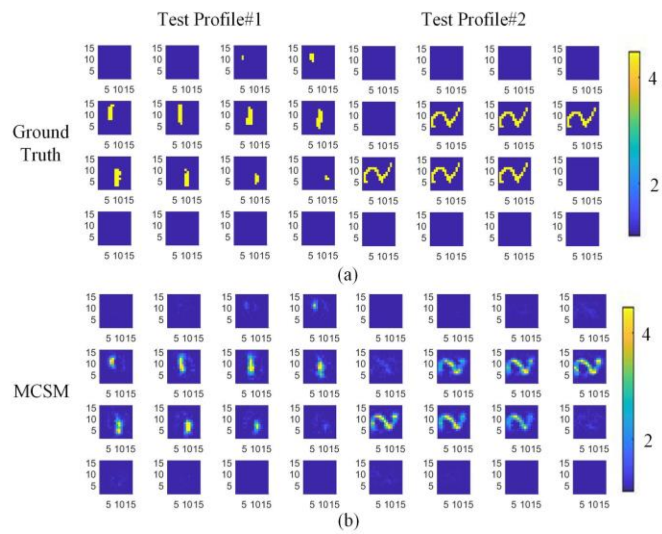

Fig. 13. Sectional view of reconstructed 3D MINIST with the relative permittivity range between 4.1 and 4.5. (a) Exact permittivity distribution. (b) Reconstructed permittivity distribution in the DOI. The index of sections can be found in the caption of Fig. 9.

V. Experimental Results

The measured data of ‘Diel’ and ‘Two Diel’ profiles in [38] are used to validate the proposed MCSM performance. The radius of the cylindrical object is equal to 0.015 m and the relative permittivity is 3 ± 0.3. The transmitter is rotated with a step of 10° from 0° to 350°, and the receiver is rotated with a step of 5° to receive the scattered field for each incidence. For each incidence, the minimum angle between the transmitter and the receiver is of 60°. The cylinder in ‘Diel’ profile is centered at (0 m, 0.03 m), and cylinders in ‘Two Diel’ profile are located at (0 m, 0.045 m) and (-0.012 m, -0.045 m). The operating frequency is 3 GHz. The size of DOI is 0.15×0.15 m^2. L is chosen to be 7, since the 7th singular value is about 50%

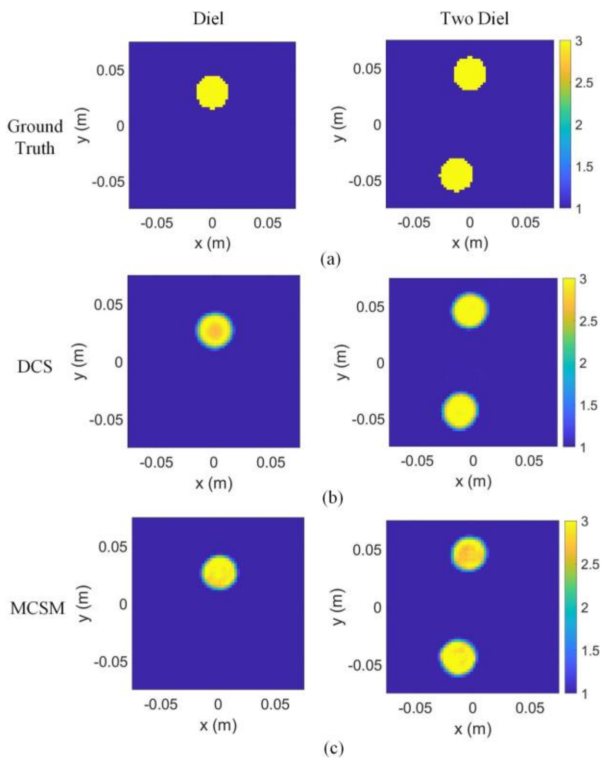

Fig. 14. Experimental profile reconstruction at 3GHz. (a) Ground truth. (b) DCS results. (c) MCSM results.

of the maximum singular value [28]. Experimental profiles are tested by the network trained by 1,000 random cylinder samples with the range of relative permittivity (2.7-3.3). R_e of 'Diel' profile is 10.68% via DCS and 10.12% via MCSM. R_e of 'Two Diel' profile is 16.10% via DCS and 14.01% via MCSM. Typical reconstructed results for experimental data are shown in Fig. 14.

VI. Conclusion

In this paper, an improved scheme, named MCS, is proposed to tackle nonlinear ISPs. Under the MCS scheme, both 2D and 3D real-time reconstruction results are provided via the trained U-Net learning architecture.

When reconstructing high-contrast scatterers, MCS outperforms DCS by applying the new CIE-I inversion model to generate the input for the U-Net, where the local-wave term is amplified to suppress the multiple scattering and thus the nonlinearity of the problem is reduced. Moreover, the APIC itself becomes the unknown in MCS. In this way, the computational cost of the APIC generation is avoided, and the existing error in the DPIC is remedied.

Although the U-Net adopted in MCS is an existing neural network architecture, we have proposed for the first time two input-output pairs in this paper, i.e., the MCSC and MCSM schemes. Compared with MCSC, MCSM performs better in both numerical and experimental examples with high contrast scatterers. Due to the good generalization ability of MCSM, it seems promising to apply MCSM in various testing situations. One reason for the better performance of MCSM is that the range of the modified contrast is always between 0 and 1, which makes it more suitable to be the input of the U-Net. When MCSM is used to reconstruct scatterers with high relative permittivity, this intrinsic property greatly reduces the training difficulty.

Finally, we have provided 3D inversion data using deep learning, which is rare in literature. Since most real-world ISPs are 3D ones [39], our presented 3D real-time inversion results can be chosen as a benchmark for researchers in ISP community to compare with.

References

[1] M. S. Zhdanov, *Geophysical inverse theory and regularization problems*, vol. 36. Elsevier, 2002.

[2] M. Salucci, L. Poli, N. Anselmi, and A. Massa, "Multifrequency Particle Swarm Optimization for Enhanced Multiresolution GPR Microwave Imaging," *IEEE Trans. Geosci. Remote Sens.*, vol. 55, no. 3, pp. 1305–1317, 2017.

[3] A. Abubakar, P. M. van den Berg, and J. J. Mallorqui, "Imaging of biomedical data using a multiplicative regularized contrast source inversion method," *IEEE Trans. Microw. Theory Tech.*, vol. 50, no. 7, pp. 1761–1771, 2002.

[4] S. J. Hamilton and A. Hauptmann, "Deep D-Bar: Real-Time Electrical Impedance Tomography Imaging With Deep Neural Networks," *IEEE Trans. Med. Imaging*, vol. 37, no. 10, pp. 2367–2377, 2018.

[5] R. Zoughi, *Microwave non-destructive testing and evaluation principles*, vol. 4. Springer Science & Business Media, 2000.

[6] Z. Liu, C. Li, D. Lesselier, and Y. Zhong, "Fast Full-Wave Analysis of Damaged Periodic Fiber-Reinforced Laminates," *IEEE Trans. Antennas Propag.*, vol. 66, no. 7, pp. 3540–3547, 2018.

[7] X. Chen, *Computational methods for electromagnetic inverse scattering*. Singapore: Wiley, 2018.

[8] M. Slaney, A. C. Kak, and L. E. Larsen, "Limitations of imaging with first-order diffraction tomography," *IEEE Trans. Microw. Theory Tech.*, vol. 32, no. 8, pp. 860–874, 1984.

[9] A. J. Devaney, "Inverse-scattering theory within the Rytov approximation," *Opt. Lett.*, vol. 6, no. 8, p. 374, 1981.

[10] K. Belkebir, P. C. Chaumet, and A. Sentenac, "Superresolution in total internal reflection tomography," *J. Opt. Soc. Am. A Opt. Image Sci. Vis.*, vol. 22, no. 9, pp. 1889–1897, 2005.

[11] M. T. Bevacqua, L. Crocco, L. Di Donato, and T. Isernia, "An algebraic solution method for nonlinear inverse scattering," *IEEE Trans. Antennas Propag.*, vol. 63, no. 2, pp. 601–610, 2015.

[12] T. Yin, Z. Wei, and X. Chen, "Non-Iterative Methods Based on Singular Value Decomposition for Inverse Scattering Problems," *IEEE Trans. Antennas Propag.*, vol. 68, no. 6, pp. 4764–4773, Jun. 2020.

[13] W. C. Chew and Y. M. Wang, "Reconstruction of two-dimensional permittivity distribution using the distorted Born iterative method," *IEEE Trans. Med. Imaging*, vol. 9, no. 2, pp. 218–225, 1990.

[14] X. Ye and X. Chen, "Subspace-Based Distorted-Born Iterative Method for Solving Inverse Scattering Problems," *IEEE Trans. Antennas Propag.*, vol. 65, no. 12, pp. 7224–7232, 2017.

[15] P. M. van den Berg and R. E. Kleinman, "A contrast source inversion method," *Inverse Probl.*, vol. 13, no. 6, pp. 1607–1620, 1997.

[16] P. M. van den Berg, A. L. van Broekhoven, and A. Abubakar, "Extended contrast source inversion," *Inverse Probl.*, vol. 15, no. 5, pp. 1325–1344, 1999.

[17] X. Chen, "Subspace-Based Optimization Method for Solving Inverse-Scattering Problems," *IEEE Trans. Geosci. Remote Sens.*, vol. 48, no. 1, pp. 42–49, 2010.

[18] Y. Zhong, M. Lambert, D. Lesselier, and X. Chen, "A new integral equation method to solve highly nonlinear inverse scattering problems," *IEEE Trans. Antennas Propag.*, vol. 64, no. 5, pp. 1788–1799, 2016.

[19] G. Oliveri, N. Anselmi, and A. Massa, "Compressive Sensing Imaging of Non-Sparse 2D Scatterers by a Total-Variation Approach Within the Born Approximation," *IEEE Trans. Antennas Propag.*, vol. 62, no. 10, pp. 5157–5170, 2014.

[20] F. Xu and M. Deshpande, "Iterative Nonlinear Tikhonov Algorithm With Constraints for Electromagnetic Tomography," *IEEE J. Sel. Top. Appl. Earth Obs. Remote Sens.*, vol. 5, no. 3, pp. 707–716, Jun. 2012.

[21] P. Shah, U. K. Khankhoje, and M. Moghaddam, “Inverse scattering using a joint $L1$-$L2$ norm-based regularization,” *IEEE Trans. Antennas Propag.*, vol. 64, no. 4, pp. 1373–1384, 2016.

[22] Y. Zhong and K. Xu, “Contraction Integral Equation for Three-Dimensional Electromagnetic Inverse Scattering Problems,” *J. Imaging*, vol. 5, no. 2, p. 27, 2019.

[23] P. Rocca, M. Donelli, G. L. Gragnani, and A. Massa, “Iterative multi-resolution retrieval of non-measurable equivalent currents for the imaging of dielectric objects,” *Inverse Probl.*, vol. 25, no. 5, p. 055004, 2009.

[24] R. Guo, X. Song, M. Li, F. Yang, S. Xu, and A. Abubakar, “Supervised Descent Learning Technique for 2-D Microwave Imaging,” *IEEE Trans. Antennas Propag.*, vol. 67, no. 5, pp. 3550–3554, May 2019.

[25] A. Massa, D. Marcantonio, X. Chen, M. Li, and M. Salucci, “DNNs as Applied to Electromagnetics, Antennas, and Propagation—A Review,” *IEEE Antennas Wirel. Propag. Lett.*, vol. 18, no. 11, pp. 2225–2229, 2019.

[26] Z. Wei and X. Chen, “Physics-Inspired Convolutional Neural Network for Solving Full-Wave Inverse Scattering Problems,” *IEEE Trans. Antennas Propag.*, vol. 67, no. 9, pp. 6138–6148, 2019.

[27] L. Li, L. G. Wang, F. L. Teixeira, C. Liu, A. Nehorai, and T. J. Cui, “DeepNIS: Deep Neural Network for Nonlinear Electromagnetic Inverse Scattering,” *IEEE Trans. Antennas Propag.*, vol. 67, no. 3, pp. 1819–1825, Mar. 2019.

[28] Z. Wei and X. Chen, “Deep-Learning Schemes for Full-Wave Nonlinear Inverse Scattering Problems,” *IEEE Trans. Geosci. Remote Sens.*, vol. 57, no. 4, pp. 1849–1860, Apr. 2019.

[29] H. M. Yao, W. E. I. Sha, and L. Jiang, “Two-Step Enhanced Deep Learning Approach for Electromagnetic Inverse Scattering Problems,” *IEEE Antennas Wirel. Propag. Lett.*, vol. 18, no. 11, pp. 2254–2258, Nov. 2019.

[30] Y. Sanghvi, Y. Kalepu, and U. K. Khankhoje, “Embedding Deep Learning in Inverse Scattering Problems,” *IEEE Trans. Comput. Imaging*, vol. 6, pp. 46–56, 2020.

[31] G. Chen, P. Shah, J. Stang, and M. Moghaddam, “Learning-Assisted Multimodality Dielectric Imaging,” *IEEE Trans. Antennas Propag.*, vol. 68, no. 3, pp. 2356–2369, Mar. 2020.

[32] J. Xiao, J. Li, Y. Chen, F. Han, and Q. H. Liu, “Fast Electromagnetic Inversion of Inhomogeneous Scatterers Embedded in Layered Media by Born Approximation and 3-D U-Net,” *IEEE Geosci. Remote Sens. Lett.*, Early Access, 2019, doi: 10.1109/LGRS.2019.2953708.

[33] O. Ronneberger, P. Fischer, and T. Brox, “U-Net: Convolutional Networks for Biomedical Image Segmentation,” *Medical Image Computing and Computer-Assisted Intervention – MICCAI 2015*, Cham, 2015, pp. 234–241.

[34] S. Fu, T. Wang, Y. Tsao, X. Lu, and H. Kawai, “End-to-End Waveform Utterance Enhancement for Direct Evaluation Metrics Optimization by Fully Convolutional Neural Networks,” *IEEE/ACM Trans. Audio Speech Lang. Process.*, vol. 26, no. 9, pp. 1570–1584, Sep. 2018.

[35] D. Kingma and J. Ba, “Adam: A Method for Stochastic Optimization,” *Int. Conf. Learn. Represent.*, Dec. 2014.

[36] Y. Lecun, L. Bottou, Y. Bengio, and P. Haffner, “Gradient-based learning applied to document recognition,” *Proc. IEEE*, vol. 86, no. 11, pp. 2278–2324, 1998.

[37] Ö. Çiçek, A. Abdulkadir, S. S. Lienkamp, T. Brox, and O. Ronneberger, “3D U-Net: learning dense volumetric segmentation from sparse annotation,” *Medical Image Computing and Computer-Assisted Intervention – MICCAI 2016*, Athens, Greece, 2016, pp. 424–432.

[38] K. Belkebir and M. Saillard, “Testing inversion algorithms against experimental data,” *Inverse Probl.*, vol. 17, no. 6, pp. 1565–1571, 2001.

[39] X. Chen, Z. Wei, M. Li, and P. Rocca, “A Review of Deep Learning Approaches for Inverse Scattering Problems,” *Prog. Electromagn. Res.*, vol. 167, pp. 67–81, 2020.

Yulong Zhou was born in Xi’an, China, in July 1993. He is currently pursuing a Ph.D. degree from the Department of Electrical and Computer Engineering, National University of Singapore, Singapore. His research interests include electromagnetic inverse scattering and directly applying it on non-destructive imaging.

Yu Zhong was born in Guangdong, China. He received the B.S. and M.S. degrees in electronic engineering from Zhejiang University, Hangzhou, China, in 2003 and 2006, respectively, and the Ph.D. degree in electrical and computer engineering from the National University of Singapore, Singapore, in 2010. He was a Research Engineer and a Fellow with the National University of Singapore from 2009 to 2013, where he was involved in the French-Singaporean MERLION Cooperative Program. Since 2014, he has been a Scientist with the Institute of High Performance Computing, Agency for Science, Technology and Research, Singapore. Since 2012, he has been regularly invited to the Laboratoire des Signaux et Systèmes, Gif-sur-Yvette, France, as an Invited Senior Scientific Expert. In June 2018, he was invited to the ELEDIA Research Center, University of Trento, as a Visiting Professor. His current research interests include numerical methods for inverse problems associated with waves and fields, electromagnetic/acoustic modeling with complex materials, and nondestructive testing.

Zhun Wei is a tenure-track assistant professor at College of Information Science and Electronic Engineering, Zhejiang University. He was a Postdoctoral Fellow in Center for Advanced Imaging, Faculty of Arts and Sciences at Harvard University from 2019 to 2020 and also a Visiting Postdoc in Stanford University from 2018 to 2019. He received the B.S. degrees in University of Electronic Science and Technology of China, in 2012, and the Ph.D. degree in National University of Singapore, in 2016. He is a recipient of 2016 Best Student Paper Competition Award, IEEE Singapore MTT/AP Joint Chapter, a recipient of “Ulrich L. Rohde Innovative Conference Paper Award” at ICCEM 2019, and a recipient of “Best Presentation Award for Oral Presentation” at NUS ECE GSS 2015. Dr. Wei is an Associate Editor of Progress In Electromagnetics Research (PIER) and also serves as Technical Program Committee Member 2019 International conference APMC and 2020 IEEE MTT-S international conference NEMO. Since 2016, Dr. Wei has published more than 30 Journal and conference papers on related topics. His research interest focuses on electromagnetic inverse problem, and directly applying it on smart medical information, information retrieval, and non-destructive imaging. His work about deep learning on inverse scattering problem is highlighted as ESI Hot paper & Highly Cited paper.

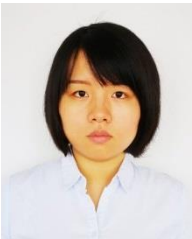

Tiantian Yin received the B.E. degree with first class honors from School of Electrical and Electronic Engineering, Nanyang Technological University, Singapore, in 2016. She is currently pursuing a Ph.D. degree from the Department of Electrical and Computer Engineering, National University of Singapore, Singapore. Her research interests include electromagnetic inverse scattering problems.

Xudong Chen (Fellow, IEEE) received the B.S. and M.S. degrees in electrical engineering from Zhejiang University, China, in 1999 and 2001, respectively, and the Ph.D. degree from the Massachusetts Institute of Technology, Cambridge, MA, USA, in 2005. Since 2005, he has been with the National University of Singapore, Singapore, where he is currently a Professor. He has published 160 journal papers on inverse scattering problems, material parameter retrieval, microscopy, and optical encryption. He has authored the book *Computational Methods for Electromagnetic Inverse Scattering* (Wiley-IEEE, 2018). His research interests include mainly electromagnetic wave theories and applications, with a focus on inverse problems and computational imaging. He is recently working on mm-wave imaging algorithms and solving inverse problems via machine learning. Dr. Chen was a recipient of the Young Scientist Award by the Union Radio Scientifique Internationale in 2010 and a recipient of the "Ulrich L. Rohde Innovative Conference Paper Award" at 2019 IEEE ICCEM conference. He was an Associate Editor of the *IEEE Transactions on Microwave Theory and Techniques* during 2015-2019 and has been an Associate Editor of the *IEEE Journal of Electromagnetics, RF and Microwave in Medicine and Biology* since 2020. He has been members of organizing committees of more than 10 conferences, serving as General Chair, TPC Chair, Award Committee Chair, etc. He was the Chair of IEEE Singapore MTT/AP Joint Chapter in 2018. He is a Fellow of Electromagnetics Academy.